A method for 3D reconstruction of volcanic bomb trajectories

Karim Kelfoun, Andrew Harris, Martial Bontemps, Philippe Labazuy, Frédéric Chausse, Maurizio Ripepe, Franck Donnadieu

A method for 3D-reconstruction of volcanic bomb trajectories

Karim Kelfoun[1], Andrew Harris[1], Martial Bontemps[2], Philippe Labazuy[1], Frédéric Chausse[3], Maurizio Ripepe[4], Franck Donnadieu[1]

1. Université Clermont Auvergne, CNRS, IRD, OPGC, Laboratoire Magmas et Volcans, F-63000 Clermont-Ferrand, France.
2. Université Clermont Auvergne, Observatoire de Physique du Globe de Clermont-Ferrand, F-63000 Clermont-Ferrand, France.
3. Université Clermont Auvergne, Institut Pascal, F-63000 Clermont-Ferrand, France.
4. Department of Earth Science, University degli Studi di Firenze, Italy.

ORCID numbers of the authors:

Karim Kelfoun	0000-0002-9289-3023
Martial Bontemps	0000-0002-4912-216X
Philippe Labazuy	0000-0002-4518-3328
Frédéric Chausse	0000-0001-7794-1587
Maurizio Ripepe	0000-0002-1787-5618
Franck Donnadieu	0000-0001-8293-1340

Email address of the corresponding author: karim.kelfoun@uca.fr

Abstract: Reconstructing bomb trajectories resulting from Strombolian activity can provide insights into near-surface dynamics of the conduit system. Typically, the high number of bombs involved represents a challenge for both automatic and manual bomb identification and tracking methods. Here, we present a method for the automated recognition of hundreds of bombs (100 to 400 depending on the explosion observed) and for the reconstruction of their trajectories in time and 3D space by stereophotogrammetry. The data involve video collected at 30 Hz with two synchronized cameras (Basler 1300-30), separated by 11°, targeting explosions at Stromboli (Aeolian Islands, Italy) in September−October 2012. In total, six data sets were collected for emissions lasting less than 15 s. The 3D reconstructions provided more accurate velocity estimations (error < 10%) than 2D analyses (errors up to 90%−100% for bombs moving parallel to the line of sight of the camera). By coupling the measured trajectories with a numerical ballistic model, we show that the method can be used to estimate the directional distribution of bombs and their velocities at the vent (which in this case was 30−130 m s^{-1}), the wind velocity (~3.5 m s^{-1} from the NW) and the drag coefficients ($10^{-3.5}$–$10^{-0.5}$) of the bombs. The 3D reconstructions also provide a quantification of the directions of explosions and show that explosions can be radial, oriented in a predominant direction of ejection or in several directions; these dispersion patterns can change during a few seconds in a single explosion. We relate the changing directions of ejections to rheological variations in the upper part of the magmatic system probably filled with a mixture of partially crystallized magma which can direct rising slugs along preferential paths.

Keywords:

3D space, stereophotogrammetry, Strombolian explosions, launch velocity, ballistic trajectory

Introduction

An in-depth understanding of volcanic activity requires a combination of modelling and field observations. Models make it possible to determine natural properties that are not accessible for direct measurement, and can be used to predict the future evolution of a natural system. To do this, field observations are used in parallel with models, to ensure that the models correctly reproduce observable parts of the natural phenomena, thus giving confidence that they can also be used for the unobservable parts and for predictions (for modelling ballistic fields see, for example, Waythomas and Mastin, 2020). For Strombolian and Vulcanian activity, bomb velocities and directions are essential parameters for calculating the distance affected by bomb impacts (Mastin, 2001), and for the understanding of the superficial activity of the magmatic system and the nature of the interactions between gas and conduit magma to generate the ensuing explosion (Wilson et al., 1980; Mastin 1995).

Velocity estimations for volcanic bombs have been previously performed using image analysis (e.g., Chouet et al. 1974, Formenti et al. 2003; Zanon et al. 2009; Vanderkluysen et al. 2012; Taddeucci et al. 2015). Manual tracking methods, suitable for a limited number of bombs, have been recently improved by automated tracking to capture a large number of bombs (Bombrun et al., 2014; Gaudin et al., 2014). However, analyses have usually been 2D, meaning that the velocities can only be estimated correctly if the bombs move solely in a plane, vertical or perpendicular to the line of sight of the camera. Volcanic ejecta generally move in diverse directions and 2D approaches can thus induce error in the estimation of bomb absolute velocities. Moreover, 2D methods cannot estimate the direction of motion of the ejecta.

More recently, 3D calculations have been performed by focusing on selected bombs using stereoscopic reconstructions derived from two synchronized cameras (Gaudin et al. 2016). The main limitations of their method was that manual tracking of pyroclasts limited the number of bombs analysed. As a further step, we present here a method for the automated recognition of hundreds of bombs and for the reconstruction of their trajectories in time and space by stereophotogrammetry.

During the course of an eruption, many thousands of bombs can be ejected (Bombrun et al., 2014). The more of these that can be tracked, the better the statistical analysis of the trajectory variations, and the greater the insight into eruptive dynamics. Tracking and identifying the bombs manually is complex, since they are launched at a range of times, angles and velocities so that at any one time thousands of different trajectories will be active. This means so bombs will be ascending while other are descending with intersecting paths, and frequently masking each other. Bombs are present over a large volume of space rather than on a planar surface, making the identification of any given bomb within images acquired from different camera positions even more difficult. To facilitate trajectory identification and 3D reconstruction, we have developed a new methodology using stereoscopic calculation based on the automated recognition of bombs. Three-dimensions reconstruction of topography has made substantial progress in recent years and has been used to follow the dynamics of natural phenomena such as glaciers, landslides and lavas flows (e.g., Eiken and Sund 2012; James and Robson, 2014; James et al, 2014; Eltner et al, 2017). Bundle adjustment (Granshaw, 1980) and recent developments that include structure-from-motion (SfM) and multi-view stereo (MVS) algorithms has widened the use of the techniques and facilitates automatic estimation of camera positions, orientations and lens characteristics. Difficulties associated with reconstructing volcanic bomb trajectories come from (1) the bomb locations that cover a large volume of space and are not restricted to a known surface, (2) the high bomb velocities that require synchronised cameras and prevent the use of a single moving cameras and (3) the high number of bombs with similar size, shape and luminosity making bomb recognition challenging in multiple

images. This explains why the bundle adjustment method has not been used for this study. Instead, we here use a custom-built 3D tracking routine.

The target chosen for the study is Stromboli volcano (Aeolian Island, Italy) because of its permanent activity characterised by discrete bursts every 5–20 mins (Chouet et al. 1974; Patrick et al. 2007), relatively easy access to the summit, and the complexity of the trajectory reconstruction related to the high number of bombs. Moreover, despite the activity of Stromboli being widely studied (e.g., Ripepe et al. 2001, Ripepe et al. 2002; Rosi et al. 2006; Harris and Ripepe 2007; Pistolesi et al. 2011; Gurioli et al. 2014), there remain open questions regarding conduit ascent dynamics and explosion mechanisms. The most frequent activity consists of repeated explosive events related to slow magma ascent in the upper conduit and/or ascent of bubbles in a low viscosity magma (Wilson et al., 1980). Several models have been proposed based on experimental and geophysical data but a number important characteristics remain poorly constrained, such as the conduit geometry, the depth at which the explosion is triggered, and the origin of the different activity types observed at the vents (e.g., Chouet et al., 1997; Chouet et al., 2008b; Harris et al. 2008; Gurioli et al. 2014; Gaudin et al. 2017). A multidisciplinary field campaign took place during September and October 2012 to increase understanding of the normal explosive activity at Stromboli, as well as to compare the results obtained using a large set of observational techniques (Harris et al. 2013; Bombrun et al. 2015; Chevalier and Donnadieu 2015). Among the spectrum of techniques used, a system of stereoscopic cameras forming the basis of the new 3D reconstruction methodology described in this article, was deployed to improve the identification of ejecta trajectories in space and time.

Methodology

System characteristics

The system comprises two digital cameras recording greyscale images from visible wavelengths (Basler 1300-30, lens Edmund Optics 8 mm F1.4). These acquire 1280- by 960-pixel images, 8 bytes per pixel, at frame rates of up to 30 frames per second, so that data acquisition rates were around 37 Mb/s for each camera. They were connected by Ethernet to the same computer to ensure that the acquisition time reference was identical for both cameras, an essential requirement for the spatial reconstruction processing stage. The positions of the two cameras were located with centimetre-accuracy using differential GPS. One camera was set to film the vent continuously and the images were analysed in real time to detect eruption occurrence (using the software Genika Trigger by Airylab). Recording was made at night to facilitate the bomb recognition: bombs appear as white on a black background. When the eruption is detected, the observing camera triggered a recording of the images from both cameras onto the computer over a period of 30 s. The triggering analysis is sufficiently fast (<20 ms) that data can be acquired from the onset periods of eruptions without an image buffer. If bombs continued to be detected, the acquisition was automatically extended by successive periods of 30 s.

The principles of a 3D reconstruction

The location of an object projection on the sensor array (i.e. the charge coupled device, CCD) within a camera depends on the position of the object in space, the camera position, the camera orientation and lens characteristics. To calculate the 3D-position of the object in real-space we thus invert this imaging model. To do this, we first need to locate the object on two images taken at the same time by the two cameras. Using a correction for the lens distortion and misalignment, we can then

calculate the undistorted position of each projection (p_1 and p_2 on Fig. 1). From the orientations of the cameras and their positions, we next calculate two lines (L_1 and L_2 on Fig. 1) that pass through each point and the optical centre of the lens (O_1 and O_2 on Fig. 1). The 3D-position of the object corresponds to the intersection of the two lines. Identifying the object on a sequence of images taken during an eruption allows a reconstruction of the trajectory to be made, i.e. in both 3D space and time.

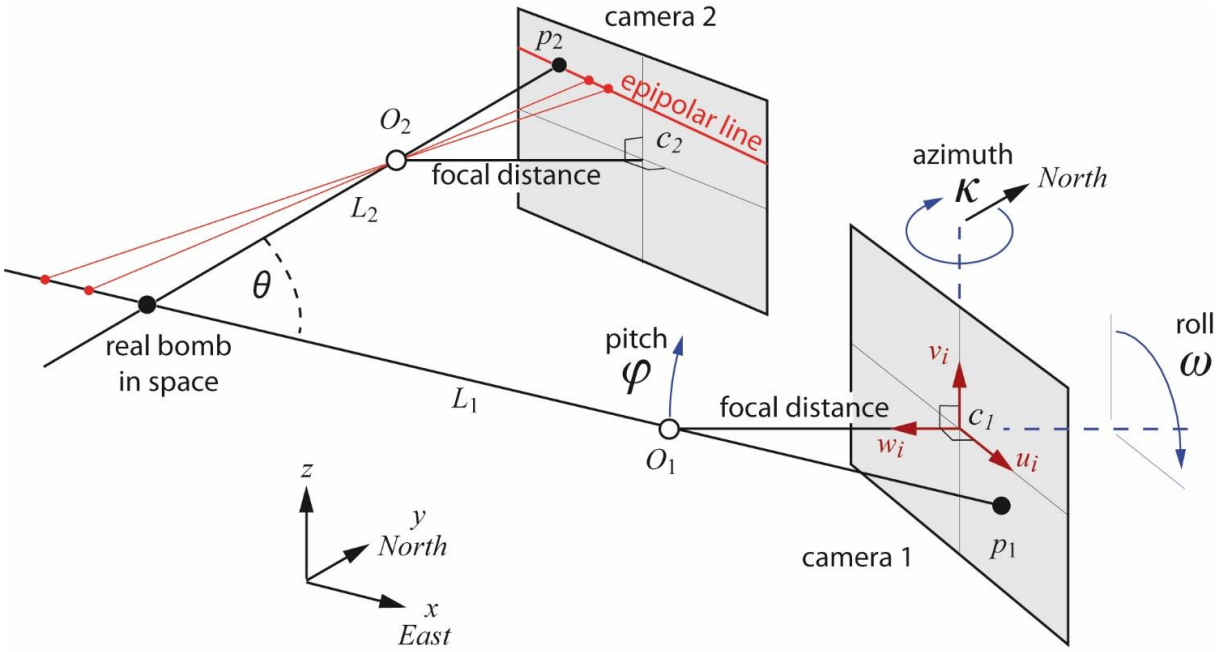

Fig. 1 Principle of position calculation by stereophotogrammetry. The 3D position of an object is calculated by the intersection of the lines L_1 and L_2 which pass by the object projections p_1 and p_2 and the optical centres of the lenses

Stereo-system geometry

At a given distance from the vent, the distance between the cameras (i.e. the baseline) is chosen based on a compromise between bomb identification, practical aspects, and precision of the 3D-reconstruction. The greater the baseline, the larger the angle camera 1 – bomb – camera 2 (angle θ on Fig. 1). If θ is very small, errors in camera orientation or subpixel uncertainty in the object detection can induce large errors in the calculation of the 3D-position. The system was installed around 430 m east of Stromboli's NE crater (Fig. 2) chosen for the study. In this configuration, with an angle θ of 2°, an error of 1 pixel induces an error in the bomb position of up to 6 m. The most accurate calculation would be obtained for $\theta = 90°$ (an error of 1 pixel induces a 20 cm error in the bomb position). However, because an eruption can emit thousands of bombs per second, a strong difference in the view angles (i.e. large values of θ) gives very different images on the two cameras. This makes bombs impossible to recognise visually, and makes some steps of our bomb identification method more complex (e.g. the auto calibration of camera orientations – see next section - is simpler if supervised). Thus, the smaller the distance between the two cameras, the easier it is to match the bombs. Given the above considerations, we estimated the ideal angle θ of about 10°. For the observation distance of about 430 m and for installation convenience, we chose a distance of 81.6 m that corresponds to an angle between the positions of the cameras and of the crater of about 11°. The system is convergent (Fig. 1) and the angle between the optical axes of the cameras (i.e. their lines of sight) is 9°. In this configuration, an error of

1 pixel in the bomb location on the image induced an error of about 1 m in the East-West direction (called *x* in the following) and less than 30 cm in North-South (*y*-direction) and in elevation (*z*-direction). The error is higher in the East-West direction because of the positions and the orientations of the cameras (to the West).

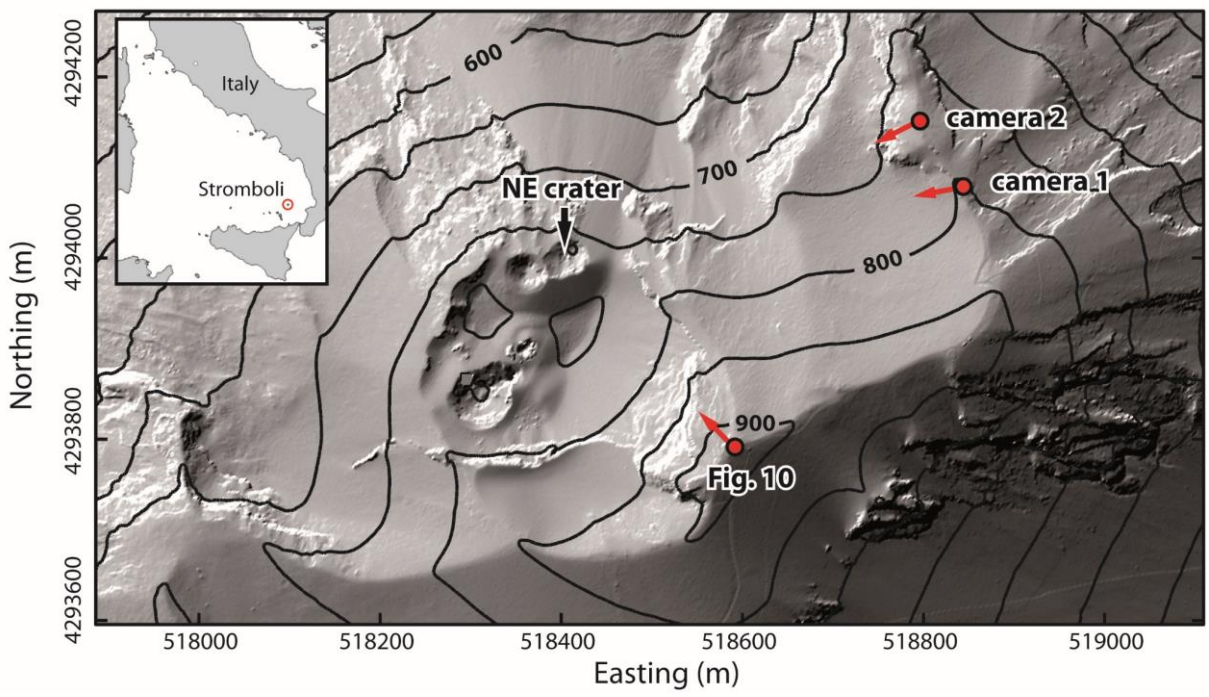

Fig. 2 Location of the NE crater, of the two cameras used for observation of ejecta trajectories and of the photograph of Fig. 10, Stomboli, Italy, 2012. Lidar-derived DEM courtesy of INGV-Pisa (Favalli et al., 2009)

Due to the distance chosen to observe the crater and the camera characteristics, each pixel in an individual image (also called the ground sample distance) corresponds to an area about 20 cm in width and height at the crater location. This, in principle, determines the minimum detectable bomb size but hot bombs much smaller than the pixel size could still illuminate the pixel and hence be detected at night.

Lens distortions

In order to calculate bomb positions accurately, the image distortions induced by the camera lenses need to be corrected. The corrections are done with the Brown–Conrady equation (Brown, 1966):

$$\begin{cases} x_{cor} = x_n\left(1+k_1\times r+k_2\times r^2+k_3\times r^4\right)+2\times q_1\times x_n\times y_n+q_2\times\left(r^2+2\times x_n{}^2\right) \\ y_{cor} = y_n\left(1+k_1\times r+k_2\times r^2+k_3\times r^4\right)+2\times q_2\times x_n\times y_n+q_1\times\left(r^2+2\times y_n{}^2\right) \end{cases} \quad (1)$$

where x_{cor} and y_{cor} is the corrected position, x_n and y_n is the uncorrected normalized position calculated by $x_n=\left(x_p-x_c\right)/f$ and $y_n=\left(y_p-y_c\right)/f$. The variables x_p and y_p are the uncorrected image

position in pixels, f is the calibrated focal length (Fig. 1; Granshaw 2016), $r = \sqrt{x_n^2 + y_n^2}$ is the distance between the position to be corrected and the position (x_c, y_c) of the principal point (i.e. the intersection between the optical axis and the CCD, c_1 and c_2, Fig. 1), and q_1, q_2, k_1, k_2, k_3 are the distortion correction parameters. Note that the principal point is not generally located at the geometric centre of the image due to lens distortion and lens misalignment. The distortion parameters, the position of the principal point and the calibrated focal length were calculated using adapted grids and protocols of the *Institut Pascal* based on the work of Lavest et al. (1999). The calibration was done in laboratory with a distance of the calibration target of 3 meters and the same focus as used in the field. Lens distortions caused differences of up to 30 pixels at the edges of the images between the corrected and uncorrected positions. The standard deviation of the correction has been calculated by comparing the parameters of Eq 1 to parameters obtained with other sets of images. It is of less than 0.3 pixel. The codes used for the reconstruction, including that for lens distortions, are available in Online Resource 1.

Orientation of the cameras

We used three angles to define our cameras (Granshaw 2016): φ is the pitch, i.e. the angle between the horizontal and the optical axis of the camera, where $\varphi>0$ means that the camera is pointing upwards (Fig. 1). The angle κ defines the azimuth, i.e., the orientation of the optical axis in the horizontal plan, where $\kappa=0$ means that the camera is oriented to the North, and $\kappa>0$ is rotated to the east. The angle ω defines the roll, i.e. the rotation around the optical axis, with $\omega>0$ for a counter-clockwise tilt of the camera.

If $\varphi=0$, $\kappa=0$ and $\omega=0$, the orientation of the camera is defined by $X_{ini} = \begin{pmatrix} u_i \\ v_i \\ w_i \end{pmatrix} = \begin{pmatrix} 1 & 0 & 0 \\ 0 & 0 & -1 \\ 0 & 1 & 0 \end{pmatrix}$, which conveys that the camera is horizontal and pointing northward, u_i and v_i defining respectively the orientation of the horizontal and the vertical for the images (CCD sensor is vertical if the camera is horizontal, Fig. 1) and w_i defining the orientation of the optical axis of the camera. The rotation matrices are:

$$R_\varphi = \begin{pmatrix} 1 & 0 & 0 \\ 0 & \cos\varphi & -\sin\varphi \\ 0 & \sin\varphi & \cos\varphi \end{pmatrix},\ R_\kappa = \begin{pmatrix} \cos\kappa & 0 & \sin\kappa \\ 0 & 1 & 0 \\ -\sin\kappa & 0 & \cos\kappa \end{pmatrix} \text{ and } R_\omega = \begin{pmatrix} \cos\omega & -\sin\omega & 0 \\ \sin\omega & \cos\omega & 0 \\ 0 & 0 & 1 \end{pmatrix} \quad (2)$$

Using theses matrices and these references, the orientation of the camera can be calculated by:

$$X = R_\omega \times R_\varphi \times R_\kappa \times X_{ini} \quad (3)$$

Calculating the camera orientation on an active volcano can be challenging. The common method consists of placing ground control points (GCP), with accurately measured positions, in the camera's field of view (Diefenbach et al, 2012). Using the images of the GCP, in combination with the lens characteristics, allows the camera orientations to be calculated. However, placing GCPs on active volcanoes is often impossible for security and accessibility reasons. To solve this problem, we used a two-step process, first calculating the approximate orientation of the camera using the surface of the sea

and the volcano topography, then improving the relative orientation of the cameras using the positions of selected bombs on the images.

For the first step we used high-resolution topography (lidar topography, resolution 1 m, Favalli et al. 2009) and calculated its projection on the CCD sensors as well as the projection of the sea surface. The projection depends on the values of φ, κ and ω, and the angles were adjusted by fitting the projections on the real images (the sea and the topography were visible on the first images taken after sunset). For details, the readers may refer to Online Resource 1 and 2 for numerical codes and an explanation of the methodology respectively. The angles φ and ω could be estimated using the sea surface, which appeared clearly and sharply on images, and can be located with a precision of less than 2 pixels. Such a precision of the sea surface gives a precision better than 0.2° for φ and ω. The calculation of κ was carried out using the digital topography (except for crater area which has evolved over time due to volcanic activity). The precision is better than 1°. Such precision in the angles (φ +/- 0.2°, ω +/- 0.2° and κ +/- 1°) induces uncertainties in the bomb locations of less than ± 10 m in *y* and *z* and about 100 m in *x* (i.e. East-West direction). In the second step, to improve the precision of the relative orientations of the cameras and of the bomb locations, we manually matched 30 volcanic bombs which could be recognized unambiguously in the two cameras. The image of each bomb projected on the first camera must be located on the second camera along a line, called epipolar, which is defined by the orientations and positions of the cameras (Fig. 1). It was then possible to find the best relative orientation of the two cameras by using a least squares minimisation of the distances between all 30 bombs on the second camera with their corresponding epipolar lines. The precision of the angles is better than 0.1°, the method mainly improving the precision of κ.

Trajectory reconstruction for a single camera

For trajectory reconstruction, the first step was to identify the maximum number of bombs on all images corresponding to a given eruption. To locate the maximum of bombs and minimize false detections, we used the algorithm written by Crocker and Grier (Crocker et al. 1996), and Blair and Dufresne (see Online Resource 1). It suppresses pixel noise and long-wavelength image variations to detect circular objects and locate their centres from their luminosity. This was made easier when image acquisition was carried out at night so that bombs appeared as bright pixels on a black background. More than 1000 bombs can be detected unambiguously on an image.

The second step was to follow all the identified bombs on the successive images of each camera. We developed our own algorithm for counting and tracking the rise and fall of bombs because no tracking algorithm available was found to be adapted to the complexity of bomb trajectories. The values of the arbitrary parameters given here have been estimated by several tests, retaining the values that give the greatest number of correct trajectories. Starting from each detected bomb in the first image of a given camera, the algorithm first initialises the trajectory by detecting all bombs in the next image from the same camera that are not 'too far' from its initial position. A distance of 100 pixels, that can detect all bombs of velocities slower than 300 m s^{-1}, gives the best results for the explosions studied (see detect_trajectories in Online Resource 1 for details). At this stage, hundreds of trajectories are possible for a given bomb. Then, for each trajectory, the algorithm estimates the position of the bomb on the third image by extrapolation of its position on the previous two images. It detects if a bomb with similar brightness (i.e. the bomb luminosity must be greater than 20% of the luminosity of the bomb initially detected) exists in the third image in the neighbourhood of the estimated position (5 pixels, i.e. ~1.5 m

between the estimated and the real positions). If no bomb exists, the trajectory is deleted. If a bomb is detected, it extrapolates the position onto the fourth image and so on until the end of the sequence. Once a trajectory has been identified by more than 10 consecutive positions, it is fixed and the algorithm will ignore the absence of a bomb within a subsequent image to take into account the fact that bombs can be hidden by others or by an ash cloud. At this stage, the algorithm has only detected the trajectories of the bombs visible on the first image. To allow the detection of trajectories of bombs that were not present or were hidden on the first image, the algorithm starts again from the second image, then from the third and so on. Trajectories that have already been detected are not recorded again. An example of a trajectory reconstruction is shown on figure 3 for more than 1600 unambiguous bomb trajectories. A movie of the eruption with superimposed trajectories and the related code are provided in Online Resource 1 and 3.

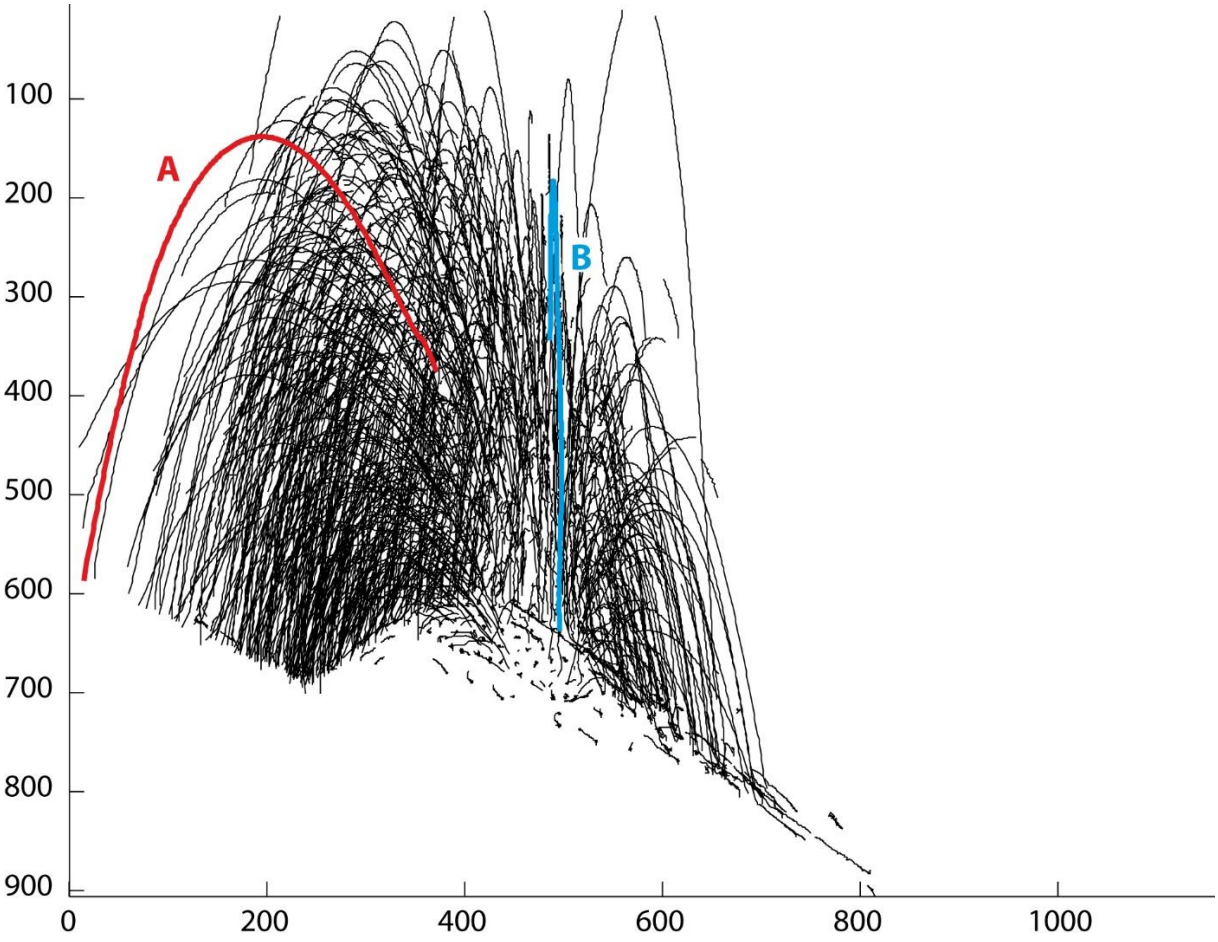

Fig. 3 Example of a trajectory reconstruction. More than 1600 bomb trajectories are identified unambiguously. The coloured trajectories A and B are used as examples in the text. Eruption of 17:20 UT, on October 5, 2012, taken by camera 2 (location shown on Fig. 2). Axes are the image distance in pixels

Trajectory matching between the two cameras

In order to calculate the real position of bomb trajectories in space, we need to match all the pairs of trajectories that correspond to similar bombs. Some bombs are easy to identify due to their size, brightness or position, but overall matching is very difficult (and often impossible to do manually).

The first step is to account for the short delay (<20 ms, i.e. 2 m for a bomb moving at 100 m s^{-1}) between image acquisition at the two cameras due to the second being triggered by the first. With the cameras connected to the same computer, the delay value is known and can be used to interpolate the trajectories of the second camera to estimate the bomb positions at the same time as the images of the first camera.

The automated method we have developed for trajectories matching is illustrated by the animation and a tutorial code in Online Resource 1 and 4. It first selects a bomb in the first image. Using its epipolar line, it is then possible to estimate which of the bombs observed in the second image it may be. To allow for errors in the camera orientations, in distortion corrections and in trajectory fluctuations, an uncertainty of 5 pixels around the epipolar line is accepted for the bomb matching. Continuing this process for all the images over the time sequence, we could identify the matching trajectory, i.e. the trajectory of camera 2 whose bombs are always on the epipolar lines of the selected trajectory of camera 1. However, due to the high number of trajectories, this method can give non-unique solutions, particularly for short trajectories close to the crater. We then filter the solution by calculating the 3D shape of the trajectory in space (see next section). A match is rejected if the calculated trajectory does not originate from the crater area and if the estimated value for gravity is outside an acceptable range. A range of 8 m s^{-2} to 12 m s^{-2} is chosen so as not to eliminate trajectories that could have been influenced by wind, blast explosion, collisions, etc. If several trajectories still match the chosen trajectory, we discard them even though it might still have been possible to identify the most probable corresponding trajectory by analysing errors in the epipolar calculation and the gravity value. We also discard trajectories that are too short. As a conservative result, only 10% to 20% of the total trajectories is retained in order to improve the chance to delete all the false matching trajectories. For example, at 17:20, about 1600 2D-trajectories have been reconstructed for each camera (Fig. 3) but only 230 have been retained for 3D reconstruction and hundreds of correlations, being non unique with the accuracy chosen, have been discarded.

3D reconstruction

The last step is based on classic 3D reconstruction. Using camera positions and orientations, lens characteristics and the matching trajectories, it is possible to calculate the position of each bomb at each time step following the principle of Fig. 1 (see also Gaudin et al. 2016). Using the recorded time of each image, we reconstructed the 3D position – in time and space – of the bombs. Due to the uncertainties in camera orientations and lens correction and in pixel locations, the lines L1 and L2 do not intersect in 3D but their closest distance of approach is generally less than 50 cm. The accuracy of the bomb positions is not easy to estimate because it is not possible to identify objects in the images whose positions have been measured by independent methods. From a comparison of the trajectories of the bombs that roll around the crater with the lidar topography, accuracy appears better than a few meters.

The precision is estimated by selecting all the matching trajectories and by calculating 10000 variations of each trajectory by adding small random offsets to the image positions, the camera orientations and distortion parameters of the lenses. The bomb images are circular and some pixels of diameter for the largest and their centres are located quite accurately. Their offsets are assumed to follow a normal distribution law with a standard deviation $\sigma = 1$ pixel in row and column. For the orientation of the cameras, the three angles of each camera follow a standard deviation $\sigma = 0.1°$. A standard deviation of 0.3 pixel is used for the uncertainties related to the distortion parameters q_1, q_2, k_1, k_2, k_3 and in the calibrated focal length. The effect on the estimated positions of the bombs in space is $\sigma \sim 4.5$

m. The standard deviation is smaller than 2 m in *y* and *z*, and of 4 m in *x* (i.e. East-West direction) due to the system geometry (Fig. 2). If the random offset is only applied to the image positions of the bomb centre, the standard deviation on the bombs in space is less than 1 m. If the random offset is only applied to the lens distortion parameters, the standard deviation on the bombs in space is less than 0.3 m. The main uncertainty is caused by the camera orientations, due to the calibration method used and the inaccessibility of the crater area that prevent the installation of ground control points.

Results

Estimation of bomb velocity using 2D and 3D trajectory reconstruction

Fig. 4 compares velocities estimated by the 2D method (assuming that the bombs move in a vertical plane passing through the crater) with those measured by our 3D reconstruction method. Two bombs from the October 5 2012 17:20 UT eruption are used as examples (throughout the article, time is given in Universal Time, UT, which corresponds to the local time minus 2 hours). One bomb moved approximately perpendicular to the lines of sight of the cameras (bomb A, Fig. 3), the other moved approximately parallel (bomb B, Fig. 3). Both methods show a deceleration of the bomb during the rising phase followed by a downward acceleration that decreased towards a constant terminal velocity when the air drag (related to the bomb velocity) equilibrates the bomb weight. On the curves shown, the bombs impacted the ground before a constant fall velocity was reached. Fig. 4 shows that the curves are not superimposed and that the error on bomb velocity incurred using the 2D assumption leads to systematic underestimations of the true velocity between 20% and 95%, the maximum error being associated with the trajectory high point. Bomb B, which moved parallel to the camera's line of sight, had a very small horizontal component of displacement on the images. For example, where it reached the highest elevation (t = 1217.15 s, Fig. 4) the 2D velocity was near to zero while the 3D analysis shows that the bomb was actually moving away from the cameras with a horizontal velocity of 5 m s^{-1}.

Characteristics of the explosions using 3D-analysis

Fig. 5 shows a 3D-view of the bomb trajectories through time for six eruptions that occurred on October 5, 2012. The trajectories reveal the highly asymmetric ejection of the largest pyroclasts as a function of time, the strong variability of jet directivity and of the maximum bomb heights among eruptions over a period of 2 hours. Fig. 6 is a plot of the maximum elevation reached by the bombs according to the azimuthal direction of their ejection. It illustrates the differences in direction and intensity between the recorded explosions. Maximal ejection heights above the vent (about 755 m a.s.l.) vary between 105 m (860 m in elevation) for the weakest eruption (i.e. 17:47) to 165 m (920 m in elevation) for the strongest (i.e. 17:20). Maximum heights tend to be reached in the predominant ejection direction (Fig. 6a, 6c) but exceptions occur (Fig. 6b).

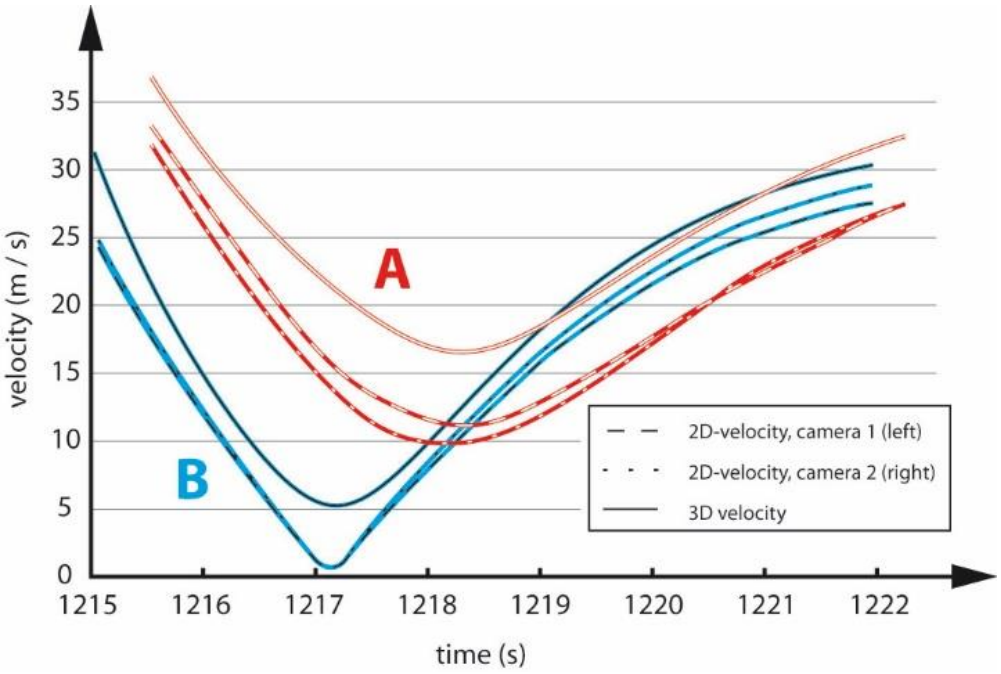

357

358 **Fig. 4** Comparison of the bomb velocities estimated using the 2D method (vertical plan passing by the
359 crater) and those calculated with the 3D reconstruction (eruption of 17:20, October 5, 2012). A and B
360 (and their respective colours) correspond to the bombs of Fig. 3

361

362 Fig. 7 links the azimuth of the ejection, the ejection time, the initial velocity (calculated in a further
363 section) and the trajectory duration. In Fig. 5d and 7d, it can be seen that during the small eruption at
364 19:00, bombs were ejected for a period of 2 s with no preferential azimuth. For the more energetic
365 eruption at 17:47 (Fig. 7c), the bombs were ejected over a wide azimuth range from south-east to north-
366 west, although with an overall predominant direction towards the south-west (azimuth, N200). This
367 predominant direction of ejection was also visible during other high energy explosions (17:04, 17:20,
368 19:12 and 19:22). For example, bombs were ejected continuously for a period of 8 s at 17:04 and again
369 at 17:20 (Fig. 7a and 7b). These two eruptions were also characterized by an initial ejection of bombs
370 with no preferential azimuth for about 1 s, before becoming predominantly oriented to the south-west.
371 The eruption at 19:22 (Fig. 7f) began with an emission predominantly oriented towards the south-west
372 for the first 7s. Two seconds after the beginning of the eruption, a number of bombs were ejected in all
373 directions. When the bomb trajectories exhibit a high directivity, the highest bomb velocities tend to be
374 recorded in the predominant ejection direction. The eruption of 19:12 had two predominant directions
375 of ejection (Fig. 5e, 6c and 7e). The eruption began with an ejection of bombs in the same direction
376 (SW) as the other eruptions for 5 s. However, two seconds after the beginning of the eruption, another
377 preferential direction of ejection joined the first, in which bombs were ejected towards the north-west
378 for 2 s. This direction of emission was detected too for other eruptions but is less clear. It can be seen at
379 17:04 on Fig. 5a, with the two short pulses recorded at 17:47 on Fig. 7c (at t = 2841 s and t = 2843 s)
380 and with few bombs ejected at 17:20 (Fig. 5b and 7b).

381

382

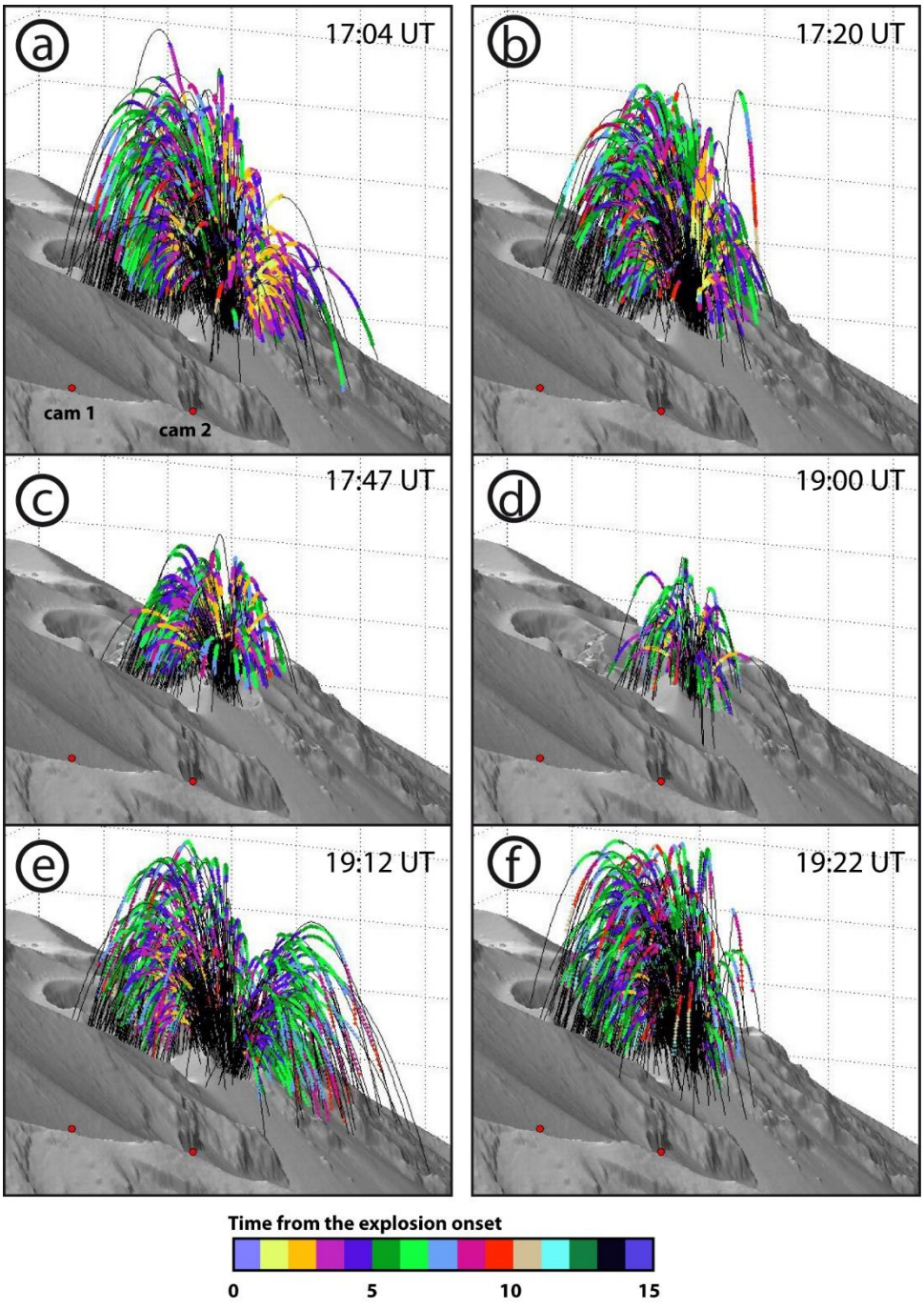

Fig. 5 3D reconstruction of the trajectories of 6 explosions on October 5, 2012. The colours indicate the time in seconds from the onset of the explosion. Black lines are parabolic fits of the trajectories

Discussion

Bomb modelling

To illustrate the potential of our 3D-reconstruction method, this section gives an example of the parameters that can be deduced by comparing a simple ballistic model with our 3D-trajectories reconstruction. Details of the model are presented in Online Resource 2. The model is simple and more

complex models have been developed (Taddeucci et al., 2017 and references therein). It is presented here only to illustrate the possibilities given by the 3D-reconstruction of trajectories. Our model calculates the bomb velocity from the Newton's First Law and the drag force exerted by the atmosphere on a bomb:

$$\frac{d\mathbf{v}}{dt} = \mathbf{g} - c \times (\mathbf{v} - \mathbf{w}) \times u \quad (4)$$

where t is time, $\mathbf{v} = (v_x, v_y, v_z)$ is the bomb velocity, $\mathbf{w} = (w_x, w_y, w_z)$, the wind velocity, $u = \|\mathbf{v} - \mathbf{w}\|$ the relative velocity between the bomb and the air and $\mathbf{g} = (0, 0, -9.81)$ is gravity in m s^{-2}. For a spherical bomb, the parameter c is defined by:

$$c = \frac{3}{8 \times r} \frac{\rho_a}{\rho} \times C_d \quad (5)$$

with ρ_a the atmosphere density, ρ the bomb density, r its radius and C_d the drag coefficient (Alatorre-Ibargüengoitia et al. 2012; Konstantinou, 2015).

By fitting the model to our 3D trajectories, we can estimate the three components of the bomb velocity (v_x, v_y, v_z) at the first detection (black dot in Fig. 8), the horizontal wind velocity (w_x and w_y) and its orientation (β_w, azimuthal origin), and the coefficient c related to the atmospheric drag on the bomb. Best fit estimations of these parameters were obtained by systematically varying the six parameters and minimizing the standard deviation between the model and the observed trajectories in both space and time. Fig. 8 shows a simulation of bomb B (see Fig. 3). For this bomb, the set of parameters that reproduces the observed data (gray line, Fig. 8) are: v_x=-7 m s^{-1}, v_y=-1.5 m s^{-1}, v_z=25.5 m s^{-1}, c=0.0055 m^{-1}, w = 3.5 m s^{-1}, β_w = -55° (wind from NW). The effects of misestimating the projection positions of the bombs and the camera orientations are dominantly accommodated by translations of the trajectories. This is why, even in the worst cases, the errors are low for the above values. They are estimated to be less than 10% for velocities and the drag coefficient, by varying the bomb positions, the camera angles and the lens distortion parameters with the normal laws of the 3D reconstruction section.

By using the values obtained for the parameters v_x, v_y, v_z, c, w and β_w, and inverting the time, we can determine the initial velocity and the initial direction of each bomb at the vent. The fitting between the measured trajectories and the model can be done automatically for all bombs detected during an eruptive phase. Fig. 9a is a histogram of the initial bomb velocities of the 17:20 eruption. The majority of the bombs were ejected at a velocity of 50 m s^{-1}, with the velocities ranging from 30 to 130 m s^{-1}. At the crater where the bombs are ejected nearly vertically, the 3D characterisation improves only the velocity estimation of less than 10% compared to 2D methods. The 3D method is, however, a powerful tool for the estimation of ejection velocities if the bomb cannot be observed directly at the vent.

Modelling of the 3D-trajectories is also a powerful tool for estimating the drag of the bomb through the air. To illustrate the sensitivity of the model to the parameter c, two other curves are added to the initial curve (c=0.0055 m^{-1}) on Fig. 8 with values of c = 0.01 m^{-1} and c = 0.0025 m^{-1}. Fig. 9b is a histogram of the coefficient c calculated for all the bombs of the 17:20 eruption. The coefficient ranges between 5×10^{-4} ($10^{-3.25}$) and 0.25 m^{-1} ($10^{-0.6}$). To first order, the histogram can be used to estimate the size distribution of the bombs from Equation 5. If, for example, we assume a value of C_d=0.7, which

has been estimated for natural bombs (Alatorre-Ibargüengoitia and Delgado-Granados 2006; de'Michieli Vitturi et al. 2010) and a bomb density of 1800 kg m^{-3} (e.g., Gurioli et al. 2013; Bombrun et al 2015; Lautze and Houghton 2007; Harris et al. 2013), a value of c = 10^{-3} m^{-1} corresponds to a radius of 14.6 cm. The bomb radii corresponding to C_d = 0.7 and ρ = 1800 kg m^{-3} are plotted on Fig. 9b. They range between <1 mm and >30 cm. Note that, below 64 mm down to 2 mm, the term lapilli must be used instead of bomb, and ash below 2 mm. It should also be pointed out that it seems unlikely for the smallest size particles of the histogram (in particular ash < 1 mm) to be sufficiently radiative to be detectable with a pixel size (i.e., a ground sample distance) of 20 cm. The sizes given are dependent on the assumptions about the bomb/lapilli density and the drag coefficient. A particle with a low density, and a complex shape and roughness might show the same coefficient *c* as a smaller particle with the density chosen and the spherical shape used for the example. A strong deceleration, comparable to that of a small particle, can also be observed for a larger particle leaving a gas jet above the crater. Our method of 3D-reconstruction can be used with more complete numerical models that would take into account these parameters.

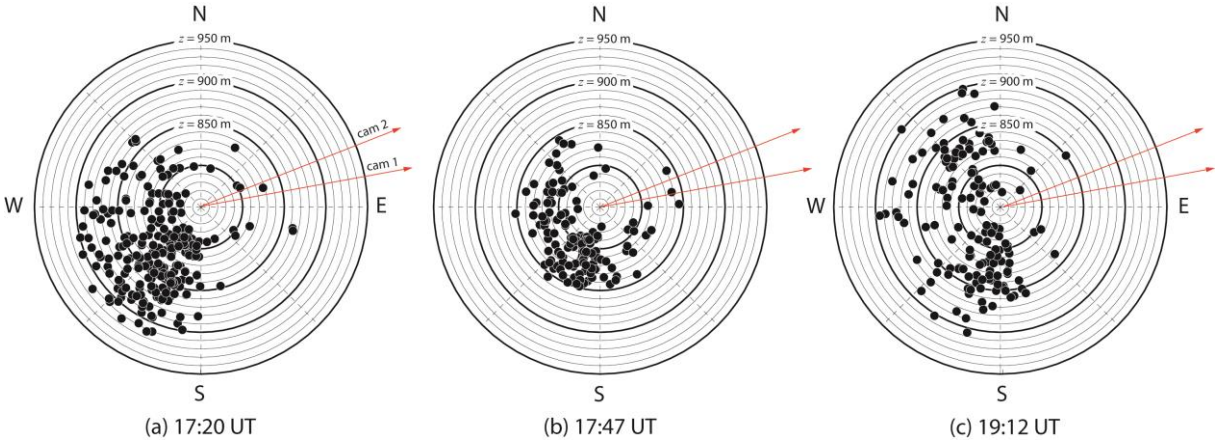

Fig. 6: Maximal elevation reached by the bombs and azimuthal direction of ejections. The elevation of the NE crater in October 2012 was about 755 m a.s.l. The graphics show that the bombs were essentially ejected in a SW direction. The eruption at 19:12 was characterized by a significant amount of ejecta to the NW, a direction that is rare or absent from the other eruptions

Limitations and improvements for the method

In the future, the number of trajectories detected by our methodology can be improved by improving the camera resolution and frame rates. For example, more than 3000 trajectories were detected for each camera, but fewer than 300 bombs were identified unambiguously. The use of higher resolution cameras would improve the precision of the bomb locations, would give more precise estimation of the bomb size and would reduce bomb identification uncertainties. Higher frame rates, using high speed cameras, would also reduce uncertainties of bomb recognition and facilitate trajectory reconstruction for each camera because bomb positions would be very close on successive images. With more confidence in the recognition, selection criteria that reject some trajectories could be lowered. This would allow complex trajectories, such as those induced by bomb collisions, to be detected unambiguously (Vanderkluysen et al. 2012). Another parameter that could be improved is the dynamics of the sensor. The challenge is to be able to see the bombs in the first phase of the eruption, when the number of hot bombs is high and tends to saturate the sensor. However, if the sensitivity is too low, the

bombs that cool rapidly are not detectable. With the cameras used, it was possible to acquire images with a higher dynamic range, for example 12 or 16 bytes. However, this would have produced a very high flux of data to be transmitted and recorded (55 to 73 Mb/s), which exceeded the capability of the laptop used during fieldwork. Finally, the system could be improved by using more than two synchronized cameras around the area under observation. This would combine the advantages of easier recognition of similar bombs with the accuracy related to a wider angle of view and would highly improve bomb recognition.

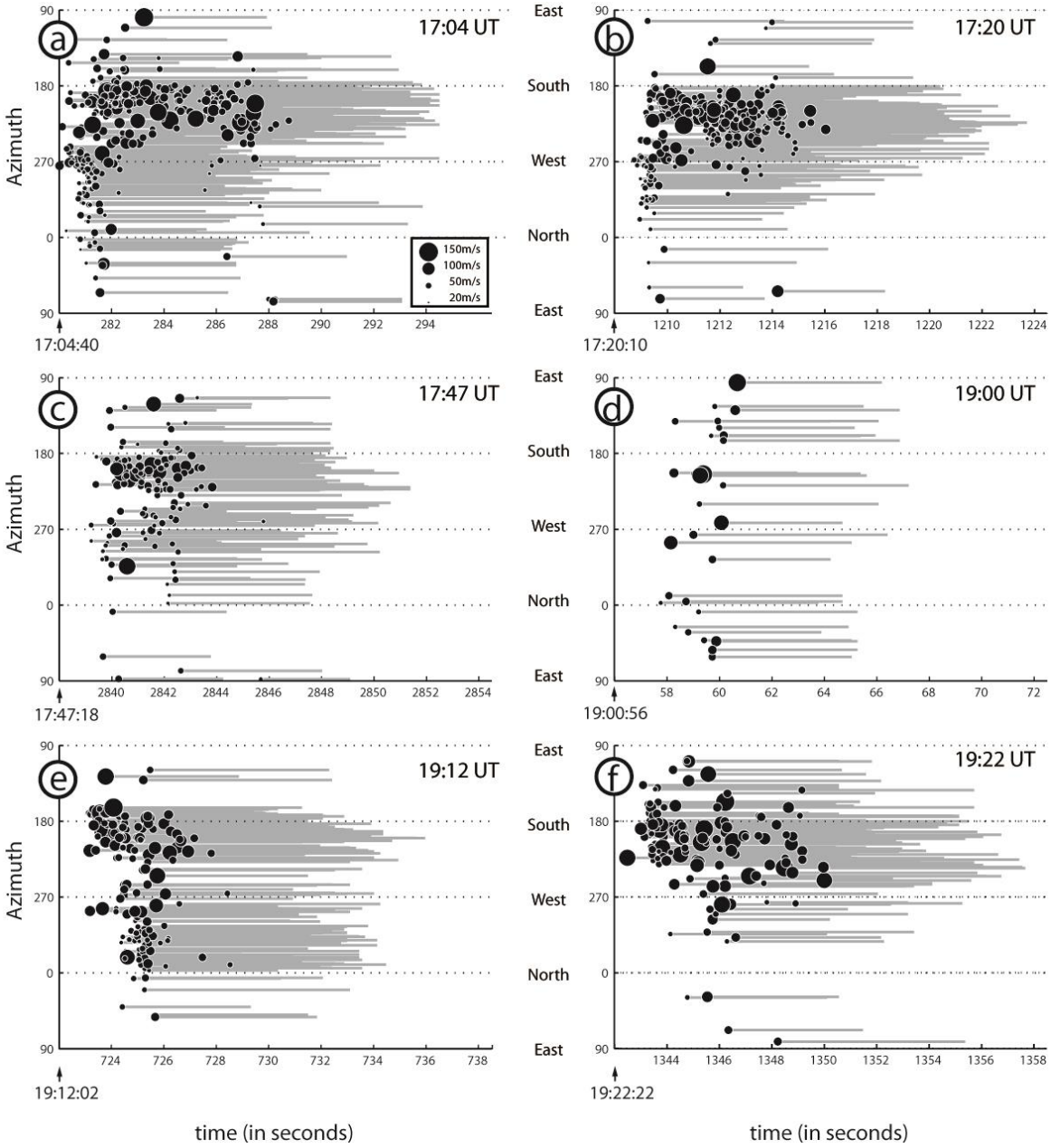

Fig. 7 Azimuth of the bomb ejection against time for the six eruptions studied on Oct. 5 2012. The horizontal axis is the time in seconds (a-c from 17:00 UT, and d-f from 19:00 UT). The black dots indicate the ejection time of each bomb and their size indicates the initial ejection velocity (see inset in 7a). The grey lines represent the time-period of the reconstructed trajectories (up to the point the bombs reach the ground, are masked by the topography or are too cooled to be detected)

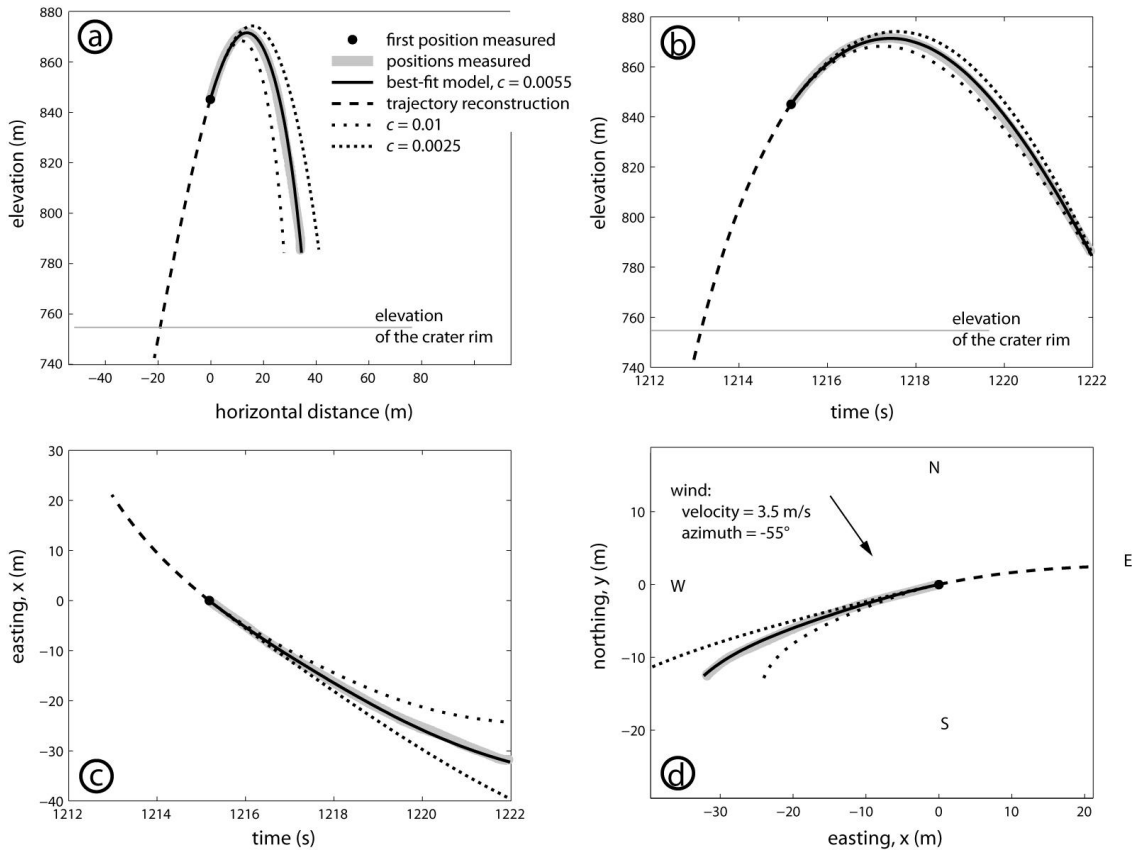

Fig. 8 Measurement of the 3D trajectory of bomb B (in grey; cf. Fig. 3) and simulations (in black) for 3 values of *c* (see Equation 8). The data are fitted in space (a, d) and time (b, c). The dashed line corresponds to the extrapolation of the bomb trajectory from its first detected position back to the vent using the best-fit values

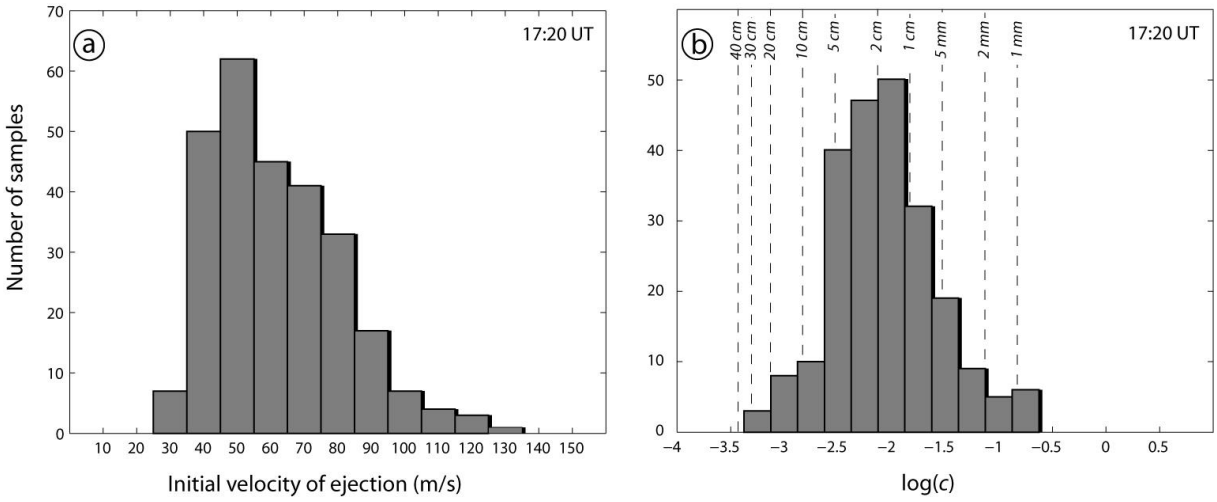

Fig. 9 (a) Histogram of calculated initial ejection velocities at the vent for the 230 bombs trajectories reconstructed during the 17:20 eruption using the model and its extrapolation. (b) Apparent drag coefficient *c* calculated using the model. The vertical lines indicate the radii corresponding to the values of *c* for *Cd*=0.7 and a bomb density of 1800 kg m^{-3}

Contribution of 3D reconstruction for conduit processes

The computed trajectories for six eruptions show a preferential direction of ejection to the south-west. It could be argued that such a direction, away from the camera, could be an artefact. Bombs ejected parallel to the line between the vent and the cameras could be more difficult to identify because of their location in the brightest area above the vent, potentially causing larger errors on their trajectories. To check if the calculated direction is correct, we have also taken photos of the same vent from the summit of Stromboli (Fig. 2). From this view angle perpendicular to the view angles of the cameras, the direction of ejection calculated, towards the south-west, is clearly confirmed (Fig. 10).

Fig. 10 Photograph of the eruption at 12:56 UT (Oct. 5, 2012); taken from the south-east (Pizzo) showing that the ejection is oriented to the SW (location of the photo on Fig. 2)

Our method might also be a useful tool for understanding conduit processes. It shows that, during the period studied, the direction of bomb ejection was either uni-directional or multi-directional and that it varied over time during an eruption and among eruptions within timescales of tens of minutes. For the eruptions at 17:04 and 17:20, the first bombs were ejected with relatively slow velocities (50 – 100 m s^{-1}) and in all directions (Fig. 7 a,b). The emissions then evolved to higher velocities with a predominant direction of ejection (N200). This is compatible with a slug of gas that reached the surface (James et al., 2004; Leduc et al., 2015). The explosions initially occurred close to the surface and they ejected bombs radially. Afterwards, the successive explosions might have become progressively deeper, and more

influenced by the orientation of the magma conduit, which seems to have been oriented N200 with a dip of about 75° (95% of the trajectories lie between 60° and 85°) during our field campaign. These values are compatible with the inclinations obtained from the locations of VLP seismic events (Chouet et al., 2008a) even if the comparison is limited by the strong morphological changes that have affected the crater area within 15 years separating our field campaigns. The smallest eruptions at 17:47 and 19:00 correspond to superficial explosions, compatible with the radial directions of the bombs. However, it appears that even during small and superficial eruptions the gas pressure can be high, based on the high velocities recorded at 19:00.

The eruption at 19:12 provides a more complete view of the superficial geometry. It began by two directions of ejection followed by a radial emission. The two directions of ejection, recorded to a lesser extent at 17:04 (Fig. 5a), can hardly be explained by a simple conduit geometry. The explanation could be that the directions of the explosions are controlled by the rheology of the superficial magma and its spatial distribution. The upper part of the conduit may be clogged by pyroclasts (Capponi et al., 2016) and is probably filled with a mixture of vesicular and denser, partially crystallized and degassed magma (e.g. Lautze and Houghton 2007; Burton et al. 2007; Bai et al. 2011; Gurioli et al. 2014). The latter can form static zones representing more difficult pathways, so that the preferential path of the rising slugs would be around the edges of the degassed magma zones. An upper conduit that broadened towards the surface, the top of which is partially obstructed by lava clots recycled from previous explosions in variable amount and conditions, might explain how explosions could occur simultaneously in many different orientations (Fig. 11). Perturbations of the static magma, rising of other slugs, or variations in the slug properties (viscosity, gas content) downwards could explain how a radial explosion occurred 3 s after the beginning of the directed explosions.

Conclusion

We have developed a system of synchronised cameras for the automated reconstruction of hundreds of volcanic bomb trajectories in 3D in space plus time. The synchronization, done by connecting the cameras to the same computer, is essential for the study of high velocity phenomena. The reconstructed trajectories, coupled with a ballistic model, allows deduction of bomb particle sizes (given shape and density assumption) from their drag coefficients and to calculate their initial velocities at the vents as well as their directions of ejection. Alternatively, if particle size is known, the drag coefficient can be used to solve for shape and/or density. The trajectories reveal the time and space variations in velocities and directions within single explosive events as well as between successive explosions. Their interpretation is compatible with preferential paths of slugs, which can become focused at the edges of the upper part of the conduit probably due to formation of a central viscous cap. Our method thus represents a tool allowing insights into superficial magmatic conditions and their relation with particle dynamics. It also provides calibration data for future techniques developed for emission dynamics characterisation, such as the Doppler radar method (Gouhier and Donnadieu, 2008).

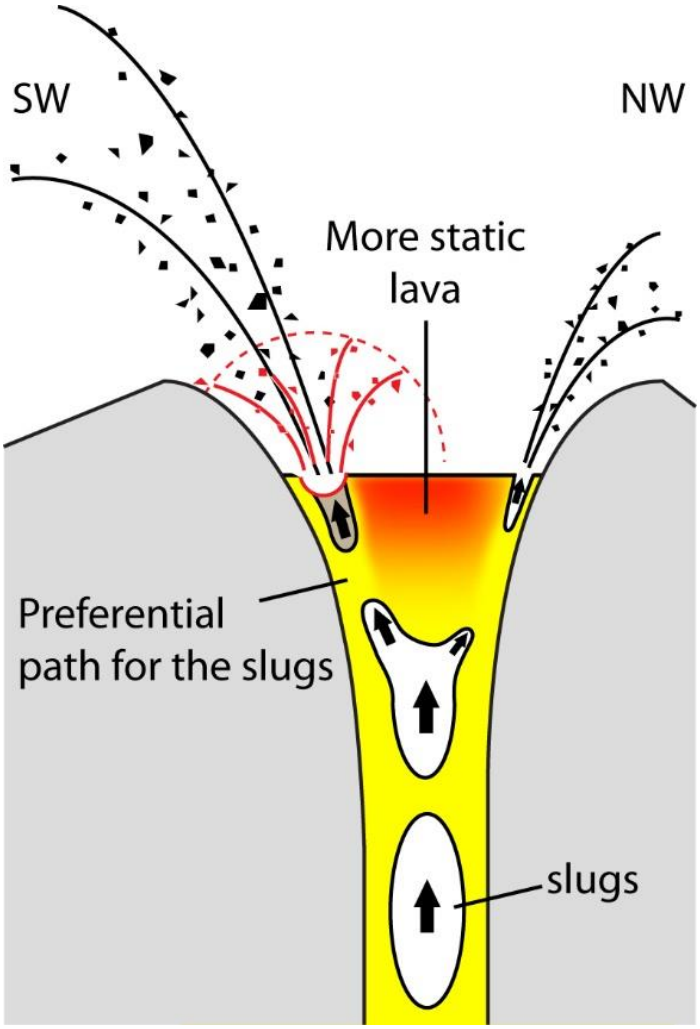

Fig. 11 A possible scheme of the upper conduit of Stromboli compatible with the bomb trajectories observed. Radial ejections (red) can be explained by explosions near the surface. With time, the slug bursts at increasing depth, focusing the directions of ejections. The various directions observed may indicate heterogeneities in the magma rheology that can form more than a single path for the slugs

Acknowledgements

The multidisciplinary mission was funded by the Laboratory of Excellence ClerVolc (contribution number 393), the *Chaire d'Excellence de la region Auvergne* and the *Observatoire de Physique du Globe de Clermont-Ferrand*. The development of the stereoscopic system was funded by the Volcanology group at the *Laboratoire Magmas et Volcans*. We thank JL Piro for sharing his experience on camera synchronisation and F Jabet, director of the Airylab company (http://airylab.fr/), for his readiness to help and for having modified the Genika trigger software for our needs. We thank S. Valade, M. Bombrun, G. Sawyer, C. Hervier, the italian DPC and Helijet for their help in the field. The manuscript was improved by the relevant comments of two anonymous reviewers and of the Associate Editor, M. R. James.

References

Alatorre-Ibargüengoitia MA, Delgado-Granados H (2006) Experimental determination of drag coefficient for volcanic materials: calibration and application of a model to Popocatépetl volcano (Mexico) ballistic projectiles. Geophys Res Lett 33:11. https://doi.org/10.1029/2006GL026195

Alatorre-Ibargüengoitia MA, Delgado-Granados H, Dingwell DB (2012) Hazard map for volcanic ballistic impacts at Popocatépetl volcano (Mexico). Bull Volcanol 74: 2155–2169. https://doi.org/10.1007/s00445-012-0657-2

Bai L, Baker DR, Polacci M, Hill RJ (2011) In-situ degassing study on crystal-bearing Stromboli basaltic magmas: Implications for Stromboli explosions. Geophys Res Lett 38, L17309. https://doi.org/10.1029/2011GL048540.

Bombrun M, Barra V, Harris A (2014) Algorithm for particle detection and parameterization in high-frame-rate thermal video. J Appl Remote Sens 8 (1), 083549. https://doi.org/10.1117/1.JRS.8.083549

Bombrun M, Harris AJL, Gurioli L, Battaglia J, Barra V (2015) Anatomy of a Strombolian eruption: Inferences from particle data recorded with thermal video. J Geophys Res Solid Earth 120: 2367–2387. https://doi.org/10.1002/2014JB011556

Brown DC (1966) Decentering distortion of lenses, Photogrammetric Engineering, 32 (3) 444–462.

Burton MR, Mader HM, Polacci M (2007) The role of gas percolation in quiescent degassing of persistently active basaltic volcanoes. Earth Planet Sci Lett 264: 46–60. https://doi.org/10.1016/j.epsl.2007.08.028

Capponi A, Taddeucci J, Scarlato P, Palladino DM (2016) Recycled ejecta modulating Strombolian explosions. Bull Volcanol 78, 13. https://doi.org/10.1007/s00445-016-1001-z

Chevalier L, Donnadieu F (2015) Considerations on ejection velocity estimation from infrared radiometer data: a case study at Stromboli volcano. J Volcanol Geotherm Res 302:130-140. https://doi.org/10.1016/j.jvolgeores.2015.06.022

Chouet B, Hamisevicz N, McGetchin TR (1974) Photoballistics of volcanic jet activity at Stromboli, Italy. J Geophys Res 79 (32) 4961–4976. https://doi.org/10.1029/JB079i032p04961

Chouet B, Dawson P, Martini M (2008a) Upper conduit structure and explosion dynamics at Stromboli. In: Calvari S, Inguaggiato S, Puglisi G, Ripepe M, Rosi M (eds) The Stromboli volcano: an integrated study of the 2002–2003 eruption. AGU, Washington, pp 81–92. https://doi.org/10.1029/182GM08

Chouet B, Dawson P, Martini M (2008b) Shallow-conduit dynamics at Stromboli Volcano, Italy, imaged from waveform inversions, S.J. Lane, J.S. Gilbert (Eds.), Fluid Motions in Volcanic Conduits: A Source of Seismeic and Acoustic Signals, Vol. 307 of Geol. Soc. Spec. Publ., The Geological Society, pp. 57-84. https://doi.org/10.1144/SP307.5

Crocker JC, Grier DG (1996) Methods of Digital Video Microscopy for Colloidal Studies. J Colloid Interface Sci 179, 298. https://doi.org/10.1006/jcis.1996.0217

de'Michieli Vitturi M, Neri A, Esposti Ongaro T, Lo Savio S, Boschi E (2010) Lagrangian modeling of large volcanic particles: Application to Vulcanian explosions. J Geophys Res Solid Earth 115: B8. https://doi.org/10.1029/2009JB007111

Diefenbach AK, Crider JG, Schilling SP, Dzurizin D (2012) Rapid, low-cost photogrammetry to monitor volcanic eruptions: an example from Mount St. Helens, Washington, USA. Bull Volcanol 74: 579. https://doi.org/10.1007/s00445-011-0548-y

Eiken T, Sund M (2012) Photogrammetric methods applied to Svalbard glaciers: accuracies and challenges. Polar Res., 31, 18671. https://doi.org/10.3402/polar.v31i0.18671

Eltner A, Kaiser A, Abellan A, Schindewolf M (2017) Time lapse structure from motion photogrammetry for continuous geomorphic monitoring. Earth Surf. Process. Landforms, 42(14): 2240-2253. https://doi.org/10.1002/esp.4178

Favalli M, Fornaciai A, Pareschi MT (2009) LIDAR strip adjustment: Application to volcanic areas. Geomorphology 111: 123–135. https://doi.org/10.1016/j.geomorph.2009.04.010

Formenti Y, Druitt TH, Kelfoun K (2003) Characterisation of the 1997 Vulcanian explosions of Soufrière Hills Volcano, Montserrat, by video analysis. Bull Volcanol 65(8):587–605. https://doi.org/10.1007/s00445-003-0288-8

Gaudin D, Moroni M, Taddeucci J, Scarlato P (2014) Pyroclast Tracking Velocimetry: A particle tracking velocimetry-based tool for the study of Strombolian explosive eruptions. J Geophys Res: Solid Earth 119 (7), 5369–5383. https://doi.org/10.1002/2014JB011095

Gaudin D, Taddeucci J, Houghton BF, Orr TR, Andronico D, Del Bello E, Kueppers U, Ricci T, Scarlato P (2016) 3-D high-speed imaging of volcanic bomb trajectory in basaltic explosive. Geochem Geophys Geosyst 17 (10): 4268–4275. https://doi.org/10.1002/2016GC006560

Gaudin D, Taddeucci J, Scarlato P, del Bello E, Ricci T, Orr T, Houghton B, Harris A, Rao S, Bucci A (2017) Integrating puffing and explosions in a general scheme for Strombolian-style activity, J. Geophys. Res. Solid Earth, 122, 1860–1875. https://doi.org/10.1002/2016JB013707

Gouhier M, Donnadieu F (2008) Mass estimations of ejecta from Strombolian explosions by inversion of Doppler-radar measurements. J. Geophys. Res., 113, B10202. https://doi.org/10.1029/2007JB005383

Granshaw SI (1980) Bundle adjustment methods in engineering photogrammetry. Photogrammetric record, 10(56): 181:207. https://doi.org/10.1111/j.1477-9730.1980.tb00020.x

Granshaw, S.I. (2016) Photogrammetric terminology.Photogrammetric Record, 31(154), 210-252. https://doi.org/10.1111/phor.12146

Gurioli L, Harris AJL, Colò L, Bernard J, Favalli M, Ripepe M, Andronico D (2013) Classification, landing distribution, and associated flight parameters for a bomb field emplaced during a single major explosion at Stromboli, Italy. Geology 41, 5: 559–562. https://doi.org/10.1130/G33967.1

Gurioli L, Colò L, Bollasina AJ, Harris AJL, Whittington A, Ripepe M (2014) Dynamics of Strombolian explosions: Inferences from field and laboratory studies of erupted bombs from Stromboli volcano. J Geophys Res Solid Earth 119: 319–345. https://doi.org/10.1002/2013JB010355

Harris AJL, Ripepe M (2007) Synergy of multiple geophysical approaches to unravel explosive eruption conduit and source dynamics−A case study from Stromboli. Geochem 67: 1–35. https://doi.org/10.1016/j.chemer.2007.01.003

Harris AJL, Ripepe M, Calvari S, Lodato L, Spampinato L (2008) The 5 April 2003 explosion of Stromboli: timing of eruption dynamics using thermal data. In: Calvari S, Inguaggiato S, Puglisi G, Ripepe M, Rosi M (eds) The Stromboli volcano: an integrated study of the 2002–2003 eruption. AGU, Washington, pp 305–316. https://doi.org/10.1029/182GM25.

Harris AJL, Valade S, Sawyer G, Donnadieu F, Battaglia J, Gurioli L, Kelfoun K, Labazuy P, Stachowicz T, Bombun M, Barra V, Delle Donne D, Lacanna G (2013) Modern Multispectral Sensors Help Track Explosive Eruptions. EOS 94, 37:321–322. https://doi.org/10.1002/2013EO370001

James MR, Lane SJ, Chouet BA, Gilbert JS (2004) Pressure changes associated with the ascent and bursting of gas slugs in liquid-filled vertical and inclined conduits. J Volcanol Geotherm Res 129, 1–3, 61–82. https://doi.org/10.1016/S0377-0273(03)00232-4

James MR, Robson H (2014) Sequential digital elevation models of active lava flows from ground-based stereo time-lapse imagery. ISPRS J. Photogram. Remote Sens., 97, 160-170. https://doi.org/10.1016/j.isprsjprs.2014.08.011

James T, Murray T, Selmes N, Scharrer K, O'Leary M (2014) Buoyant flexure and basal crevassing in dynamic mass loss at Helheim Glacier. Nature Geoscience, 7. https://doi.org/10.1038/ngeo2204

Konstantinou KI (2015) Maximum horizontal range of volcanic ballistic projectiles ejected during explosive eruptions at Santorini caldera. J Volcanol Geotherm Res 301: 107–115. https://doi.org/10.1016/j.jvolgeores.2015.05.012

Lautze NC, Houghton BF (2007) Linking variable explosion style and magma textures during 2002 at Stromboli volcano, Italy. Bull Volcanol 69, 4: 445–460, https://doi.org/10.1007/s00445-006-0086-1

Lavest JM, Viala M, Dhome M (1999) Quelle précision pour une mire d'étalonnage. GRETSI Traitement du Signal, 16(3) :241–254, 1999.

Leduc L, Gurioli L, Harris AJL, Colò L, Rose-Koga, EF (2015) Types and mechanisms of strombolian explosions: characterization of a gas-dominated explosion at Stromboli. Bull Volcanol 77: 8. https://doi.org/10.1007/s00445-014-0888-5

Mastin, LG (1995) Thermodynamics of gas and steam-blast eruptions. Bull Volcano1, 57, 85– 98. https://doi.org/10.1007/BF00301399

Mastin, LG (2001) A simple calculator of ballistic trajectories for blocks ejected during volcanic eruptions. U.S. Geol. Surv. https://doi.org/10.3133/ofr0145

Patrick MR, Harris AJL, Ripepe M, Dehn J, Rothery DA, Calvari S (2007) Strombolian explosive styles and source conditions: insights from thermal (FLIR) video. Bull Volcanol 69:769–784. https://doi.org/10.1007/s00445-006-0107-0

Pistolesi M, Delle Donne D, Pioli L, Rosi M, Ripepe M (2011) The 15 March 2007 explosive crisis at Stromboli volcano, Italy: Assessing physical parameters through a multidisciplinary approach. J Geophys Res 116, B12206. https://doi.org/10.1029/2011JB008527

Ripepe M, Ciliberto S, Della Schiava M. (2001) Time constraints for modeling source dynamics of volcanic explosions at Stromboli. J Geophys Res 106, 8713–8727. https://doi.org/10.1029/2000JB900374

Ripepe M, Harris AJL, Carniel R (2002) Thermal seismic and infrasonic evidences of variable degassing rates at Stromboli volcano. J Volcanol Geotherm Res 118, 285–297. https://doi.org/10.1016/S0377-0273(02)00298-6

Rosi M, Bertagnini A, Harris AJL, Pioli L, Pistolesi M, Ripepe M (2006) A case history of paroxysmal explosion at Stromboli: Timing and dynamics of the April 5, 2003 event. Earth Planet Sci Lett 243, 594–606. https://doi.org/10.1016/j.epsl.2006.01.035

Taddeucci J, Alatorre-Ibarguengoitia MA, Palladino DM, Scarlato P, Camaldo C (2015) High-speed imaging of Strombolian eruptions: Gas-pyroclast dynamics in initial volcanic jets. Geophys Res Lett 42:6253–6260. https://doi.org/10.1002/2015GL064874

Taddeucci J, AlatorreIbargüengoitia MA, Cruz-Vázquez O, Del Bello E, Scarlato P, Ricci T (2017) In-flight dynamics of volcanic ballistic projectiles, Rev. Geophys., 55, 675–718. https://doi.org/10.1002/2017RG000564.

Vanderkluysen L, Harris AJL, Kelfoun K, Bonadonna C, Ripepe M (2012) Bombs behaving badly: unexpected trajectories and cooling of volcanic projectiles. Bull Volcanol 74:1849-1858. https://doi.org/10.1007/s00445-012-0635-8

Waythomas CF, Mastin LG (2020) Mechanisms for ballistic block ejection during the 2016–2017 shallow submarine eruption of Bogoslof volcano, Alaska. Bull Volcanol 82, 13 (2020). https://doi.org/10.1007/s00445-019-1351-4

Wilson L (1980) Relationships between pressure, volatile content and ejecta velocity in three types of volcanic explosion, J. Volcanol. Geotherm. Res. 8 (2-4), 297-313. https://doi.org/ 10.1016/0377-0273(80)90110-9

Zanon V, Neri M, Pecora E (2009) Interpretation of data from the monitoring thermal camera: the case of Stromboli volcano (Aeolian Islands, Italy). Geol Mag 146:591–601. https://doi.org/10.1017/S0016756809005937

Online Resource

Numerical codes (ESM-1), movies (ESM-3 and ESM-4), explanations (ESM-2) and images sequences of camera 1 and 2 can be downloaded from the OPGC (*Observatoire de Physique du Globe de Clermont-Ferrand*) website: http://opgc.fr/SO/televolc/stereovolc/data/Stromboli/Codes&data.html

ESM-1: simplified versions of the codes used and sample images to explain the method (2 Mo). The codes are written in Matlab and compatible with the free software Octave. Images sequences needed by the codes must be download here (80 Mo): http://opgc.fr/SO/televolc/stereovolc/data/Stromboli/Codes&data.html

ESM-2: list and description of the codes of ESM-1 and details of the numerical model.

ESM-3: movie of the bomb tracking used for the trajectories reconstruction of figure 3. Eruption of 17:20 UT, on October 5, 2012, taken by camera 2 (location shown on figure 2).

ESM-4: animated images of the method of matching trajectories. The code used, Seeks_matching_trajectory_from_epipolar.m, is given in Online Resource 1.